Bioinspired Functionally Graded Composite Assembled Using Cellulose Nanocrystals and Genetically Engineered Proteins with Controlled Biomineralization

Pezhman Mohammadi, Julie-Anne Gandier, Nonappa, Wolfgang Wagermaier, Ali Miserez, and Merja Penttilä*

Nature provides unique insights into design strategies evolved by living organisms to construct robust materials with a combination of mechanical properties that are challenging to replicate synthetically. Hereby, inspired by the impact-resistant dactyl club of the stomatopod, a mineralized biocomposite is rationally designed and produced in the complex shapes of dental implant crowns exhibiting high strength, stiffness, and fracture toughness. This material consists of an expanded helicoidal organization of cellulose nanocrystals (CNCs) mixed with genetically engineered proteins that regulate both binding to CNCs and in situ growth of reinforcing apatite crystals. Critically, the structural properties emerge from controlled self-assembly across multiple length scales regulated by rational engineering and phase separation of the protein components. This work replicates multiscale biomanufacturing of a model biological material and also offers an innovative platform to synthesize multifunctional biocomposites whose properties can be finely regulated by colloidal self-assembly and engineering of its constitutive protein building blocks.

1. Introduction

Biological materials provide a unique source of inspiration for the design of analogous next-generation high-performance materials. In particular, damage-tolerant biological structures are comprised of hard and soft components hierarchically arranged into multiphase composites with characteristic dimensions ranging from nano- to macroscopic length scales.[1–5] These complex multiscale structures endow natural biocomposites with a combination of strength, stiffness, and toughness that is crucial for their physiological functions, ranging from structural support to defense to hunting.[6–10]

The peacock mantis shrimp (*Odontodactylus scyllarus*) offers such an example in its pair of hammer-like clubs that deliver repetitive high-energy strikes during close-range hunting or combat without undergoing catastrophic failure, despite their ability to break some of the strongest marine exoskeletons, i.e., highly mineralized mollusc shells (**Figure 1**).[10,11] Detailed physico-chemical and micromechanical analyses of the club have identified the key microstructural factors bestowing it with its remarkable damage tolerance.[11,12]

The club is a multiphase composite that combines a stiff, hard and impact-resistant external region with a softer interior that provides additional dissipation of impact energy.[13] The interior region is a 3-component structure consisting of: i) fibrillar chitin organized into a highly expanded helicoidal pattern, ii) a protein-rich matrix that mediates mineralization of the club,

P. Mohammadi, M. Penttilä
VTT Technical Research Centre of Finland Ltd
VTT
Espoo FI-02044, Finland
E-mail: pezhman.mohammadi@vtt.fi

J.-A. Gandier
Department of Bioproducts and Biosystems
School of Chemical Engineering
Aalto University
P.O. Box 16100, Espoo FI-16100, Finland

⬤iD The ORCID identification number(s) for the author(s) of this article can be found under https://doi.org/10.1002/adma.202102658.

Nonappa
Faculty of Engineering and Natural Sciences
Tampere University
Korkeakoulunkatu 6, Tampere FI-33720, Finland

W. Wagermaier
Department of Biomaterials
Max Planck Institute of Colloids and Interfaces
Am Mühlenberg1, 14476 Potsdam, Germany

A. Miserez
Centre for Sustainable Materials (SusMat)
School of Materials Science and Engineering
Nanyang Technological University (NTU)
50 Nanyang Avenue, Singapore 639798, Singapore

A. Miserez
School of Biological Sciences
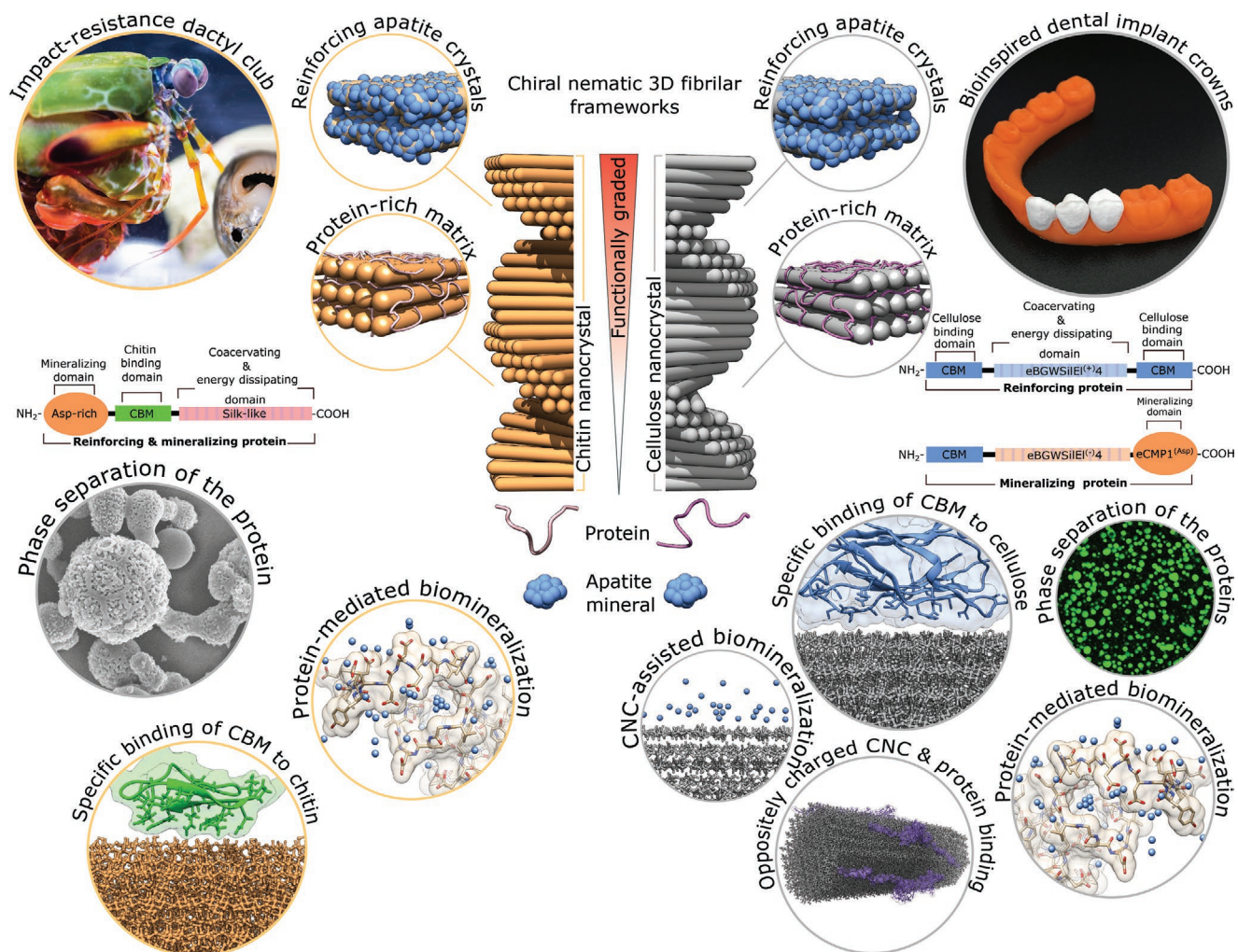60 Nanyang Drive, NTU, Singapore 637551, Singapore

Figure 1. Biologically inspired multiphase nanocomposite with a graded structure that mimics key molecular and architectural features of the mantis shrimp dactyl club.

and iii) amorphous calcium phosphate and calcium carbonate (Figure 1). In the exterior impact region, these three main components are also present but in different relative contents, organization, and polymorphic forms.

Chitin fibrils are organized in a sinusoidal pitch-graded chiral nematic structure, whereas the mineral phase is more abundant and consists of crystalline fluorapatite (FAP) nanorods.[11] The protein matrix throughout the club is thought to bind the composite together and regulate biomineralization, with the main protein (called "club mineralization protein-1", CMP-1) found to harbor both a chitin-binding domain as well as an acidic-rich domain that mediates apatite crystallization (Figure 1).[14]

The exterior and interior work synergistically to enhance the overall damage tolerance of the club.[13] While the impact region exhibits a quasi-plastic deformation associated with interfacial sliding of the nanocrystals, the interior region undergoes strain-hardening due to densification of the chitin-rich helicoidal structure.[13] This intricate, complex multilayer architectural design is not unique to the dactyl club. Other structural materials also combine a stiff outer layer with a tough inner layer, most notably human teeth.[4]

Herein, we report a new class of biologically inspired multiphase nanocomposites with a graded structure that mimics key features of the mantis shrimp dactyl club (Figure 1). We successfully fabricated a biocomposite made of analogous building blocks—namely cellulose as a replacement to chitin, artificial proteins with both cellulose binding modules (CBMs) and the acidic domain of CMP-1 regulating biomineralization, and apatite—which is strong and damage-tolerant. Furthermore, we processed this composite into intricate shapes by manufacturing it into a dental implant crown with periodic patterns of microreinforcement orientation, and a bilayer architecture similar to human teeth (Figure 1). The composite consists of cellulose nanocrystals (CNCs) with long-range helicoidal organization mixed with two types of genetically engineered protein matrices. One CBM-containing protein was rationally designed to increase its interfacial strength with the chiral nematic oriented CNC network through noncovalent interactions and is spatially located in the interior region of the crown. The second protein was designed with the acidic-rich CMP-1 in order to harden, strengthen, and stiffen the surface of oriented CNCs by mediating nucleation and growth of apatite crystals.

ADVANCED
SCIENCE NEWS
www.advancedsciencenews.com

ADVANCED
MATERIALS
www.advmat.de

2. Results and Discussion

2.1. Selection of Building-Block Components

To mimic the club's energy-absorbent multilayered helicoidal organization of chitin nanofibrils, we selected plant-derived and abundantly available colloidal CNC rods (**Figure 2**a,b) as the bulk component of the composite given their outstanding physico-chemical properties.[15–17] In particular, we selected CNC due to its impressive mechanical properties (elastic modulus ≈130 GPa and strength 3–6 GPa), low density (1.5–1.6 g cm^{-3}), low thermal expansion coefficient (5.1–6 × 10^{-4} mL g^{-1} °C^{-1}), high colloidal stability in water, and ease of processing. Furthermore, its compatibility with proteins is easily achieved.[16–20] Most importantly for our purpose, their high inter-rod affinity above a critical concentration (5–6% w/v)[21,22] results in phase separation and self-assembly into a left-handed chiral nematic (cholesteric) liquid crystal, which can be preserved upon drying (Figure 2c). Their use, however, is limited by their low fracture dissipation attributed mainly to their low aspect ratios. This limitation can be circumvented by exploiting the structural compatibility of CNCs with carbohydrate binding domain (CBD)-containing proteins. First, we set out to explore the use of reinforcing structural proteins to produce a tough fracture energy-dissipating matrix (Figure 2d and Figure S1, Supporting Information).[23–26] We hypothesized that such proteins would enable bridging interactions between the stiff long-range chiral nematic helicoidal CNC scaffold, thus acting as a molecular binder. Second, our earlier reports demonstrate that to use these proteins as a binding matrix for biocomposites, it is crucial to initially induce their phase separation and condensation into highly concentrated assemblies, often described as coacervates (Figure 2e,f and Figures S2–S6, Supporting Information).[27–30] Key advantages of concentrated coacervates include increased intermolecular interactions, low viscosity and interfacial tension, all of which greatly facilitate wetting and infiltration through the CNC network to result in strong binding to the reinforcing phase. This allowed the coacervate microdroplets to mediate the binding of CNC rods, which could not be possible in the absence of coacervation (Figure 2i).[23–26]

Furthermore, we have recently found that CMP-1 in the club of the peacock mantis shrimp has a three-block primary structure (Figure 2d)[14] that may result in all three of the characteristics required to act as a matrix of a tough biocomposite. First, it has a conserved mid-block carbohydrate-binding module that is likely used as an anchor to chitin fibrils in the club. While such modules have historically been almost exclusively described as components of carbohydrate-degrading enzymes, there is growing evidence illustrating that they also play a crucial role in the biological fabrication of high-performance structural biomaterials such as the squid beak[27] and mollusk shells[28] by forming noncovalent bridging interfaces between carbohydrates, proteins, and inorganic minerals. Second, its N-terminal contains long stretches of aspartic (Asp) acid-rich regions that are ideally suited to bind to Ca^{2+} ions and regulate apatite mineralization. Indeed, in vitro biomineralization assays demonstrated that CMP-1 could induce the formation of apatite minerals.[14] Third, the C-terminal is enriched in Glycine (Gly), Proline (Pro), and Alanine (Ala) residues and was predicted to be intrinsically disordered, a feature common to many proteins exhibiting coacervation. Accordingly, incubation of CMP-1 with Ca^{2+} ions was found to induce the formation of coacervate-like microdroplets, which may be a way to sequester and concentrate Ca^{2+} ions to accelerate the biomineralization process.[14]

Consequently, we rationally designed a set of five proteins with a three-block architecture combining these three characteristics, namely: i) a carbohydrate-binding motif; ii) a self-coacervation domain; and iii) a biomineralization domain to trigger in situ apatite crystallization (Figure 2d and Figure S1, Supporting Information). Of the set, four of the five are called reinforcing proteins (RF1-4) while the remaining one is called mineralizing protein (MP1). This segregation of functions facilitated the experimental design, systematic characterization, and ability to optimize the energy-absorbent chiral nematic CNC 3D framework independent of the mineralization process. Each protein design included a central domain consisting of a resilient structural protein with intrinsically disordered tendencies known to self-coacervate, as well as end domains conferring either binding to CNCs (i.e., CBMs) or mineralizing properties.

In RP1, we included six repeats of motif 1 of the *Eumeta variegate* silk fibroin (BGW6).[31] The central domain of RP2 is comprised of 80 repeats of the elastin-like polypeptide (ELP)_(VPGVG)$_{80}$.[32] In RP3, we used four repeats of the tandem repeat ((A)$_{25}$K(VPGVG)$_{15}$GD)$_4$,[32] which was called eSilEl. In RP4, we engineered a four-motif repeating sequence ((YKYKYKY(VPGVG)$_5$)$_3$GD(A)$_9$ K(A)$_{12}$ KSVVYV)$_4$ (named eBGWSilEl$^{(+)}$4) by combining parts of BGW6 and eSilE, and introducing a lysine- (Lys) and Tyrosine-rich (Tyr) stretch (YKYKYKY) to further enhance binding interactions with negatively charged CNCs through electrostatic interactions.

The use of flanking CBMs was adopted from our reports illustrating that the increased number of CBMs can substantially enhance the binding affinity of the proteins to cellulosic substrates. Such a design has the added advantage of increasing fibril-fibril cohesion and overall interfacial tension in the bulk, hence changing material structures and mechanical properties. Furthermore, previously we have also found that the squid beak crucially relies on multimodular flanking CBM containing proteins for its very high stiffness and strength.[28] The use of such an approach can be broadly anticipated in the design and manufacturing of other naturally occurring high-performance biological materials.

Finally, MP1, the mineralizing protein, was designed to mimic the highly mineralized hard exterior impact region of the club. It is a modified version of RP4 whereby the C-terminus CBM was replaced with the Asp-rich cluster residues 131–293 from CMP-1[14] (called eCMP1^{Asp}), and all the poly-Lys stretches of eBGWSilEl$^{(+)}$4 were mutated to glutamic acid (Glu).

2.2. Nanocomposite Assembly of Impact Resistant Interior Region of the Crown

Previously we described how a diverse set of structural proteins can undergo ion-induced liquid–liquid phase separation (LLPS) in vitro, resulting in the spontaneous formation of two immiscible liquid phases from the dispersed protein solution by loss of solvation.[24,28,33,34] In the present study, LLPS of
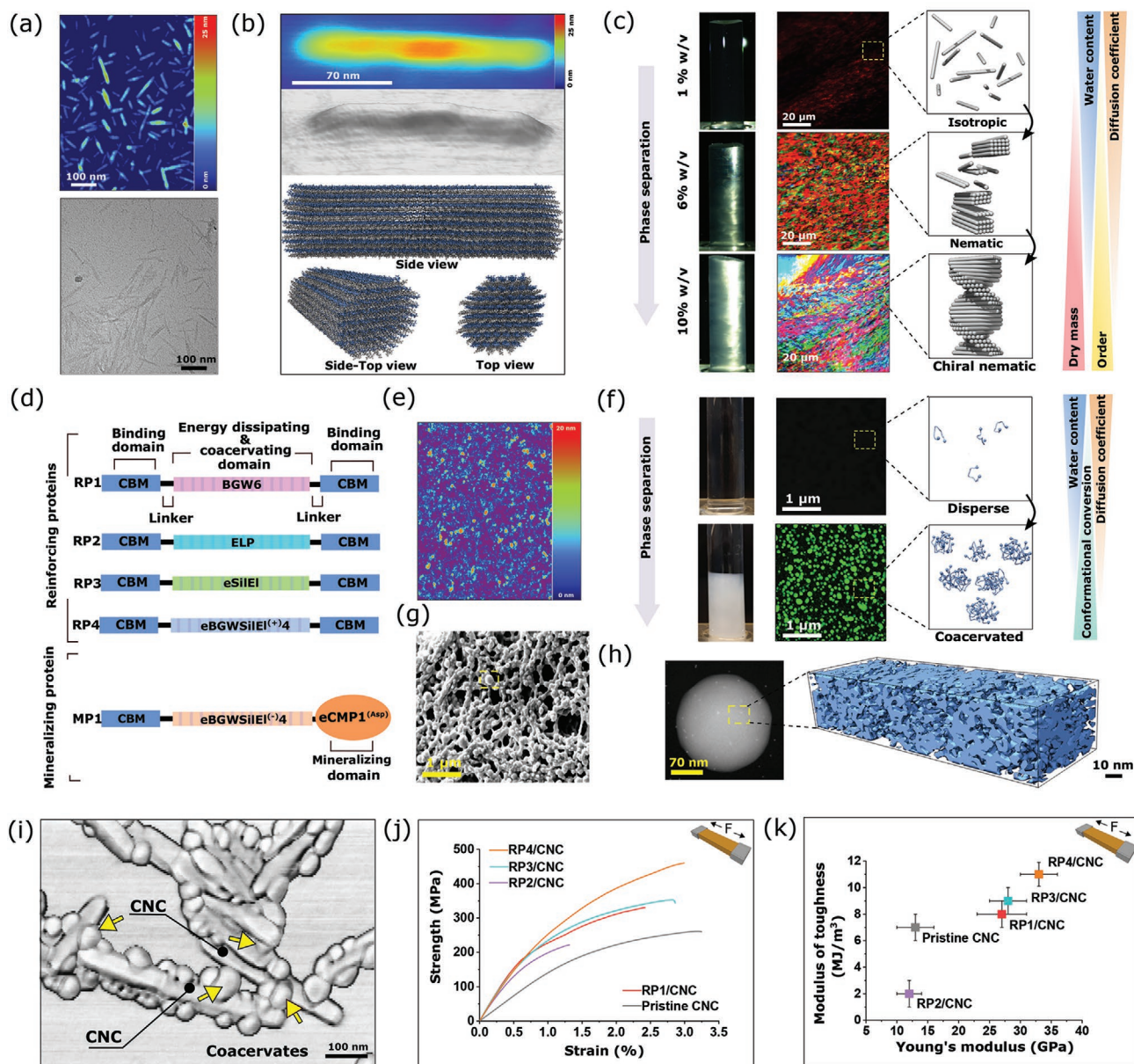
Figure 2. Engineered proteins and CNC components can be simultaneously assembled via phase separation into ultrastructures with high strength and modulus of toughness. a) Atomic force microscopy (AFM) and cryo-transmission-electron-microscopy (TEM) of pristine CNCs (1 mg mL^{-1}) with bar plot illustrating size distribution. b) High-resolution AFM image of a single CNC in height and 3D rendered topography view modes with the corresponding atomistic model. c) Phase separation and self-assembly of long-range chiral nematic helicoidal structures of CNC suspension with increasing wt%. The panel shows photographs of CNC suspensions at various concentrations viewed under cross-polarizers (left) as well as polarized microscopy images from the corresponding suspensions (middle). d) Schematic representation of the reinforcing proteins (RP1–4) and mineralizing protein (MP1). e) AFM of disperse (i.e., prior to coacervation) CBM-eBGWSilEl$^{(+)}$4-CBM protein in milli-Q water with a few clusters of weakly interacting protein monomers (2×10^{-6} M). f) Liquid–liquid phase-separation (LLPS) of CBM-eBGWSilEl$^{(+)}$4-CBM (100×10^{-6} M) after addition of kosmotropic salt (potassium phosphate 1 M). The left panels show macrophotographs and the right panels show confocal images corresponding to the two states before (top) and after (bottom) LLPS. g) Scanning electron microscopy (SEM) image of protein coacervates. h) High-resolution dark-field scanning transmission electron microscopy (STEM) of a single protein coacervate with a rectangular electron tomogram section illustrating its internal structure. i) 3D rendered topographic AFM image of intermixed coacervated CBM-eBGWSilEl$^{(+)}$4-CBM and CNCs. The coacervates that bond to the surface of CNCs are indicated by the black arrows. j) Representative tensile stress–strain curves of pristine CNC film and RP1–4/CNC composites. k) Young's modulus versus modulus of toughness for the corresponding samples shown in (j). Mean values ± standard deviation (SD) (*n* = 7) are shown.

the reinforcing proteins was initiated by mixing a solution of 1 M potassium phosphate at pH 7.4 with 100×10^{-6} M protein, resulting in a clear dilute phase on top and a dense coacervate phase on the bottom of the vial with droplet sizes in the range of 0.05–1 μm (Figure 2f–h and Figures S2–S6, Supporting Information). To assemble nanocomposite films, we intermixed

**ADVANCED
SCIENCE NEWS**
www.advancedsciencenews.com

**ADVANCED
MATERIALS**
www.advmat.de

CNC (3% w/v) with the RPs in their coacervated form (10% with respect to the dry mass of CNC). Under controlled conditions, the mixture was then concentrated to achieve the critical CNC concentration (6% w/v), after which it was allowed to fully dry into films. To evaluate the effect of individual protein variants on the mechanical properties, we performed tensile measurements (Figure 2i–k and Figure S7, Supporting Information). Compared to pure CNC, mixtures containing RP1, RP3 and RP4 displayed considerable improvement in stiffness, strength and modulus of toughness with only a minor reduction in the strain at failure (≈0.5–1%). In contrast, the mechanical response of RP2 was fundamentally different, forming a brittle material. Such dramatic differences in properties can be attributed to the lack of poly-Ala stretches in ELP's core sequence. Earlier observations have shown that Ala-rich sequences undergo conformational conversion from random coil/α-helical to a β-sheet dominated content,[23,24] which increases protein-protein interactions and results in a more cohesive matrix with more efficient load transfer. Such a molecular network creates interlocking regions that dissipate the mechanical stress between the protein chains and have been found to significantly toughen natural silk (Figure S6, Supporting Information).[31,35] This is consistent with the circular dichroism (CD) measurements showing that RP1, RP3, and RP4 all underwent a conformational transition, while RP2 retained its conformation after coacervation (Figure S3, Supporting Information). Among the RP/CNC biocomposites, RP4 showed the highest stiffness (33 ± 3 GPa), strength (460 ± 35 MPa), and modulus of toughness (11 ± 0.9MJ m^{-3}) (Figure 2i–k and Figure S7, Supporting Information). We attribute the superior mechanical properties of this biocomposite to its stronger protein/CNC binding interactions brought by the additional Lys-rich stretch that can form ionic interactions with CNC, which further enhances the CNC/CBMs affinity. Subsequent experiments were all carried out on RP4 since this fusion variant displayed the most promising mechanical performance.

It is understood that the molecular weight (MW) of a given protein can substantially alter the mechanical properties of the material both in natural and synthetic systems. In fact, this phenomenon was observed and reported in our previous work where we demonstrated the impact of protein MW on the mechanical properties of their nanofibrillated cellulose composite fibers.[23] In this particular context, we found that protein constructs with as little as a 20% smaller MW from the best performing variants resulted in composites with lower strain at break, lower strength, and toughness.[23] Given this insight, proteins were carefully designed to control for the potential impact of MW without having to produce too many variants. We rationally designed all the proteins with as similar an MW as possible resulting in a range from 69–83 KD. Maintaining the exact same MW throughout was not possible as we used seven entirely different domains to construct the five protein fusion variants. Instead, we maintained the same MW within ± 10–15 kD. When considering RP4, the best performing variant in terms of mechanical properties in this work, differences in the molecular weight are well within our established threshold. It is also important to emphasize that the N and C terminal domains of all reinforcing proteins (RP1–4) have identical folded structures. The major difference between the

reinforcing proteins variants is the amino acid arrangement and composition in the middle block. Given that the MW of RP4 is 12 KD more than the MW of RP1–3, it is not our intention to make a strong statement on the effect of MW on the mechanical properties reported. That being said, looking at the proteins with almost identical MWs (RP1, RP2, and RP3), one can see that when intermixed with cellulose nanocrystals (CNC) the resulting material has an entirely distinct mechanical response. This suggests that molecular arrangement and amino acid composition of the mid-block region may very well be more important than variation in MW with the important condition that MW falls within the defined freedom window of (10–15%) as we previously described.[23]

To gain more insight into the role of molecular interactions and relationships between molecular structure and mechanical properties, we systematically studied the effect of varying the coacervated RP/CNC mixing ratio. Upon increasing the weight ratio (at a constant CNC content of 6% w/w) we noted a clear decrease in modulus, strength and toughness (**Figure 3**a and Figure S8, Supporting Information). High-resolution SEM on the fracture surfaces of the corresponding specimens suggested qualitative differences in the orientation of CNCs in the dried films (Figure 3b). Pure CNC, as well as 10% and 20% weight ratios, showed chiral nematic ordering, while higher mixing ratios were entirely isotropic. Synchrotron wide-angle X-ray scattering (WAXS) measurements on pristine CNC 6% w/v, RP4 10%/CNC 6% w/v, and RP4 20%/CNC 6% w/v showed a four-quadrant symmetry signal with meridian and equatorial arcs for the (004) and (200) reflections. We calculated the Hermans orientation parameter (HOP) for these films from the azimuthal intensity profile of the (200) equatorial arcs, and found that HOP ranged from 0.67–0.69, indicative of a high degree of orientation. In contrast, scattering signals for all the other samples containing more than 20% RP4 had azimuthal Debye–Scherrer ring patterns (Figure 3b, Figure S9, Supporting Information) with an HOP of 0.0, illustrating no preferential orientation. In situ WAXS/SAXS structural evolution from liquid crystalline solutions to solid materials during the self-assembly and drying process followed a similar trend (Figures S10–S12, Supporting Information). Furthermore, to demonstrate that the cholesteric CNC network is preserved after the incorporation of the optimum weight ratio of RP4 (10%), we studied the hydrated samples using CD (Figure 3c). CD spectra consistently showed a clear single positive peak at 200–250 nm, illustrating left-handed chirality independent of CNC concentration (Figures S13–S15, Supporting Information). This indicates that RP4 can indeed effectively adsorb to the CNC surfaces and follows the CNCs' left-handed twist. Therefore, we conclude that there exists an optimum relative content of RP4, above which excessive addition of RP4 unfavorably results in stronger oppositely charged interfacial complexation. This can kinetically arrest CNCs from self-assembling into the chiral-nematic superstructure. Together, these data provide the foundation to formulate composites with higher CNC concentration in order to construct denser 3D bulk structures instead of 2D films without altering the protein content. Another key advantage of increasing the CNC content was that the resulting bulk material displayed a highly expanded helicoidal organization with an exceptional
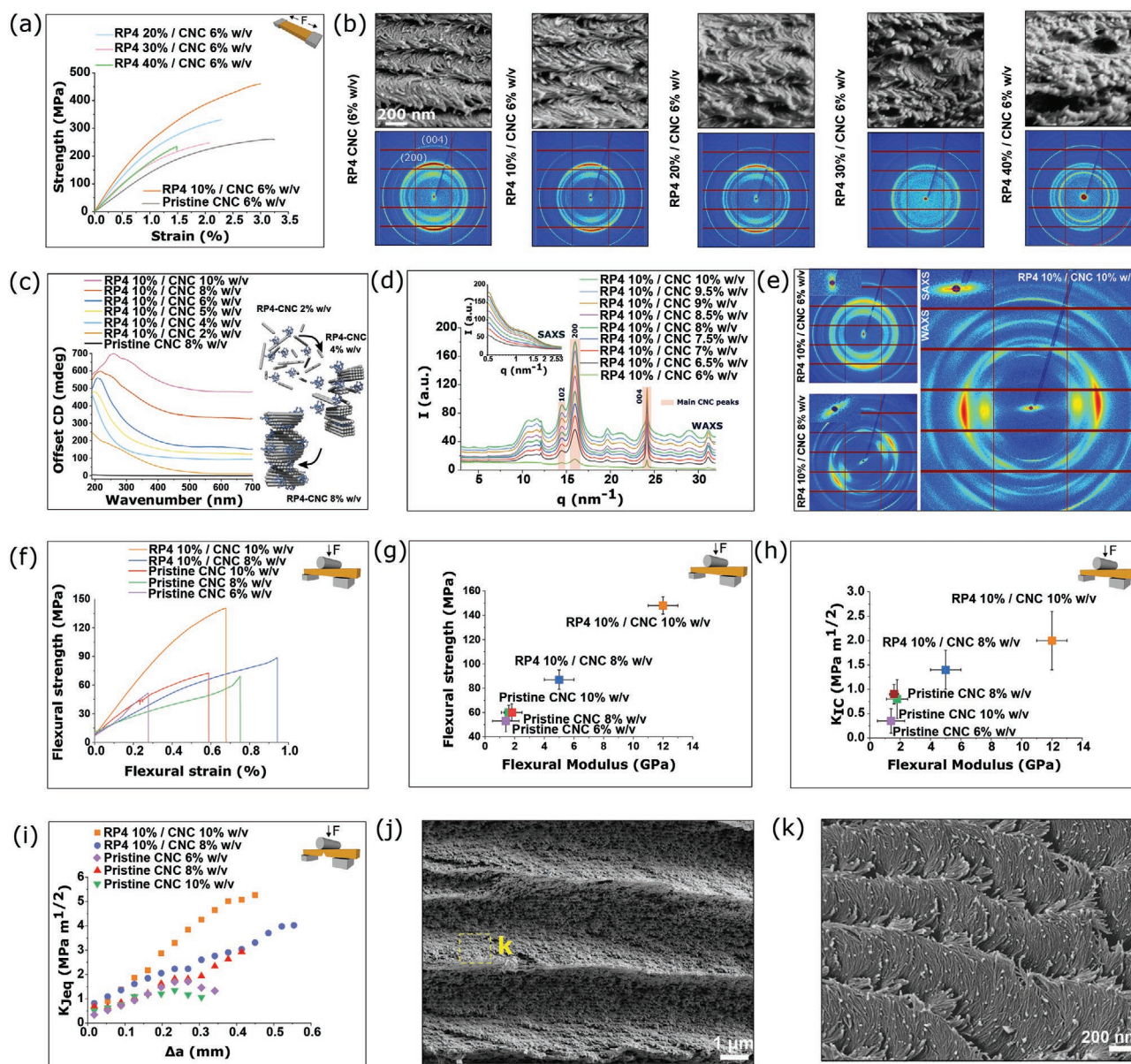
Figure 3. Optimizing fracture dissipation of CNC's chiral nematic superstructure in the composite. a) Representative tensile stress–strain curves of pristine CNC film made from 6% w/v suspension and composite films at different concentrations of the coacervated form of RP4 with respect to the total dry mass of CNCs. b) Cross-section of the corresponding films shown in (a) after cryo-fracturing under liquid nitrogen (top) and synchrotron wide-angle X-ray scattering (WAXS) patterns for the corresponding films (bottom). c) Circular dichroism (CD) spectra of RP4 mixed with chiral CNCs before drying. For all samples, the concentration of the protein is 10% with respect to the dry mass of CNCs. d) 1D synchrotron wide and small-angle X-ray scattering (WAXS/SAXS) of bulk RP4/CNC composite at various concentrations of CNCs. e) Synchrotron WAXS/SAXS patterns corresponding to (d). f) Flexural stress–strain curves of the RP4 10%/CNC 10% w/v composite and reference compositions. g) Flexural modulus versus flexural strength for the samples shown in (c). Mean values ± SD (n = 5) are shown. h) Flexural modulus versus fracture toughness at crack initiation (K_{Ic}) for the samples shown in (c). Mean values ± SD (n = 5) are shown. i) Crack-resistance curves (R-curves) showing the increase in fracture resistance (K_{Jeq}) with the crack extension (Δa). The equivalent fracture toughness at the onset of crack instability is K_{Jc}. j,k) SEM images of fractured cross-sections of bulk CNC and RP4/CNC composite after three-point flexural bending testing at low (j) and high (k) magnifications.

higher orientation parameter (Figure 3d,e and Figures S16 and S17, Supporting Information). For RP4 10%/CNC 10% w/v, HOP was found to be 0.96, ultimately leading to higher flexural strength and modulus which can be attributed to the denser arrangement of CNC rods and higher orientation degree. The ultimate flexural strength for RP4 10%/CNC 10%

w/v bulk reached a value as high as 150 MPa and a flexural modulus of about 12 GPa (Figure 3f,g).

We then assessed the fracture response of the 3D bulk composite using both linear-elastic fracture mechanics (LEFM) protocol to obtain the fracture toughness at crack initiation, as well as crack resistance curves in order to evaluate the stable crack

**ADVANCED
SCIENCE NEWS**
www.advancedsciencenews.com

**ADVANCED
MATERIALS**
www.advmat.de

propagation behavior. The initiation fracture toughness K_{Ic} was ≈2 MPa m$^{1/2}$; however, the composites did not fail in a brittle fashion. Instead, they exhibited significant *R*-curve behavior (stable crack propagation) with an equivalent fracture toughness (K_{Jeq}) reaching values as high as 5 MPa m$^{1/2}$ prior to catastrophic failure (Figure 3h,i). To obtain more insight into the fracture mechanisms, we looked at the fracture surfaces of bulk RP4 10%/CNC 10% w/v after three-point flexural tests. Cracks exhibited large in-plane periodic break patterns through crack twisting and interfacial sliding of helicoidally arranged CNC rods, very similar to fracture surface features identified in the dactyl club and suggested to be associated with the energy dissipating and toughening mechanisms (Figure 3j).[36] Moreover, we noted less delamination of CNC layers in the bulk RP4 10%/CNC 10% w/v, indicating stronger adhesion between individual CNC layers due to binding with RP4, which can delay catastrophic failure (Figure 3k and Figure S18, Supporting Information). In contrast, the pristine CNC fracture surface showed pronounced delamination and pull-outs.

2.3. Nanocomposite Assembly of a Highly Mineralized Stiff and Hard Exterior region of the Crown

The complex step of mineral formation in most biological systems is induced synergistically by highly ordered 3D fibrillar frameworks (e.g., collagen in bone or chitin in seashells) and intrinsically disordered proteins (IDPs) (e.g., Phov in bone or Pif80 in nacre). While the 3D framework guides the spatial deposition of minerals, it is believed that IDPs control the nucleation and growth of biominerals. We also observed this trend while investigating apatite mineralization in native dactyl clubs, in particular finding that CMP-1 can mediate nucleation and growth of apatite crystals on the surface of the chiral nematic chitin 3D framework.[14] CMP-1 undergoes LLPS induced by Ca^{2+} ions and we suggested that this preassembly could be a key intermediate step in the biofabrication of the club by increasing the local concentration of Ca^{2+} ions in order to accelerate the biomineralization process.[14]

To this end, we explored whether MP1, (Figure 2d) could induce biomimetic apatite mineralization on the surface of the helicoidally organized RP4/CNC 3D framework and emulate the highly mineralized external impact region of the dactyl club. We incubated MP1 for 24 d with modified simulated body fluid (SBF) (pH ≈ 7.4)[37] and probed apatite biomineralization using polarized light microscopy (PLM), a technique in which changes in birefringence and crystallinity are directly correlated (**Figure 4**a). We noted considerable differences in the birefringence intensity as a function of time, suggesting biomineralization was occurring in the form of granule-shaped precipitates. While we did not observe any noticeable birefringence in the first few days, we observed the emergence of strong birefringence after 4 d of incubation, which continuously increased until day 16 and then remained relatively unchanged. Calculating the granule size from PLM images showed a gradual increase in the size which had a direct correlation with the incubation time (Figure S21, Supporting Information)

We then collected Raman spectra of bulk mineralized specimens formed for periods of 2–16 d (Figure 4b). The spectra showed vibration peaks in the 400 to 1200 cm^{-1} wavenumber range assigned to (v_1–v_4) of PO_4^{3-} of HAP that increased in intensity with time, indicative of increasing crystallinity. Consequently, we recorded $^1H \rightarrow ^{31}P$ heteronuclear correlation (HETCOR) 2D magic-angle spin nuclear magnetic resonance (MAS-NMR), with the expectation that this would enable selective enhancement of protonated species in close proximity with phosphate ions of crystalline apatite mineral (Figure 4c and Figure S19, Supporting Information). The 16 d sample showed a relatively sharp ^{31}P signal at 1.57 ppm correlated with OH^{-1} at δ (^1H) at around 0.0 ppm corresponding to ordered PO_4^{3-} of the apatite crystallite as previously described.[38,39] In all other samples, the corresponding $^{31}P/^1H$ cross-peak was broader, indicating lower crystallinity (Figure S20, Supporting Information). Using scanning transmission electron microscopy (STEM) we then visualized specimens mineralized over 16 d (Figure 4d). STEM images showed a relatively large amount of electron-dense build-up with a size distribution in the range of 5–200 nm into large granule-shaped precipitates corresponding to the observation made by PLM (Figure 4a). Selected-area electron diffraction (SAED) analysis on these granules showed characteristic diffraction patterns matching crystalline HAP as well as an amorphous halo ring, indicating the co-existence of both amorphous and crystalline HAP. Energy-dispersive X-ray spectroscopy (EDS) mapping confirmed the presence of P, Ca, and O expected for a calcium phosphate mineral compound (Figure 4e).[40]

Subsequently, we evaluated whether the coacervated state of MP1 affected apatite formation on the surface of the 3D framework and probed both structural and mechanical properties of the resulting composite. To this end, pre-assembled RP4/CNC films were rehydrated and infiltrated with MP1, followed by a biomineralization step for 16 d. Raman spectra collected from the nonmineralized specimens exhibited only bands associated with the organic phase (protein and CNC, Figure 4f), In contrast, after biomineralization peaks corresponding to the characteristic v_4 vibrations of crystalline HAP emerged. The other vibration peaks (v_1 and v_3) could not be observed due to overlapping signals from CNC, with the exception of the infiltrated sample with the MP1 followed by the mineralization step. High-magnification SEM images illustrated the formation of a significant mineral phase on the surface of CNC rods in the RP4/CNC/MP1 specimens (Figure 4g). We noted the formation of granular-shaped clusters covering the entire surfaces of aligned CNC rods organized into planar sheets, with a size range of 5–150 nm composed of smaller granules. These clusters completely connected in-plane CNCs within a single layer and were also found between adjacent layers. Looking at the synchrotron WAXS/SAXS scattering signals we found only azimuthal Debye–Scherrer ring patterns with Herman's orientation parameter (HOP) close to 0.0, confirming no preferential orientation of templated HAPs on the surface of the anisotropic CNC-protein scaffold.

Interestingly, the formation of apatite on the surface of CNC rods did not disrupt the long-range helicoidal arrangement and resulted in a mechanical reinforcing effect. While the flexural modulus increased noticeably, the flexural strength did not change significantly and most importantly, this came at the expense of only a slight decline in specific fracture toughness (Figure 4h,i). The composite prepared with MP1 in the
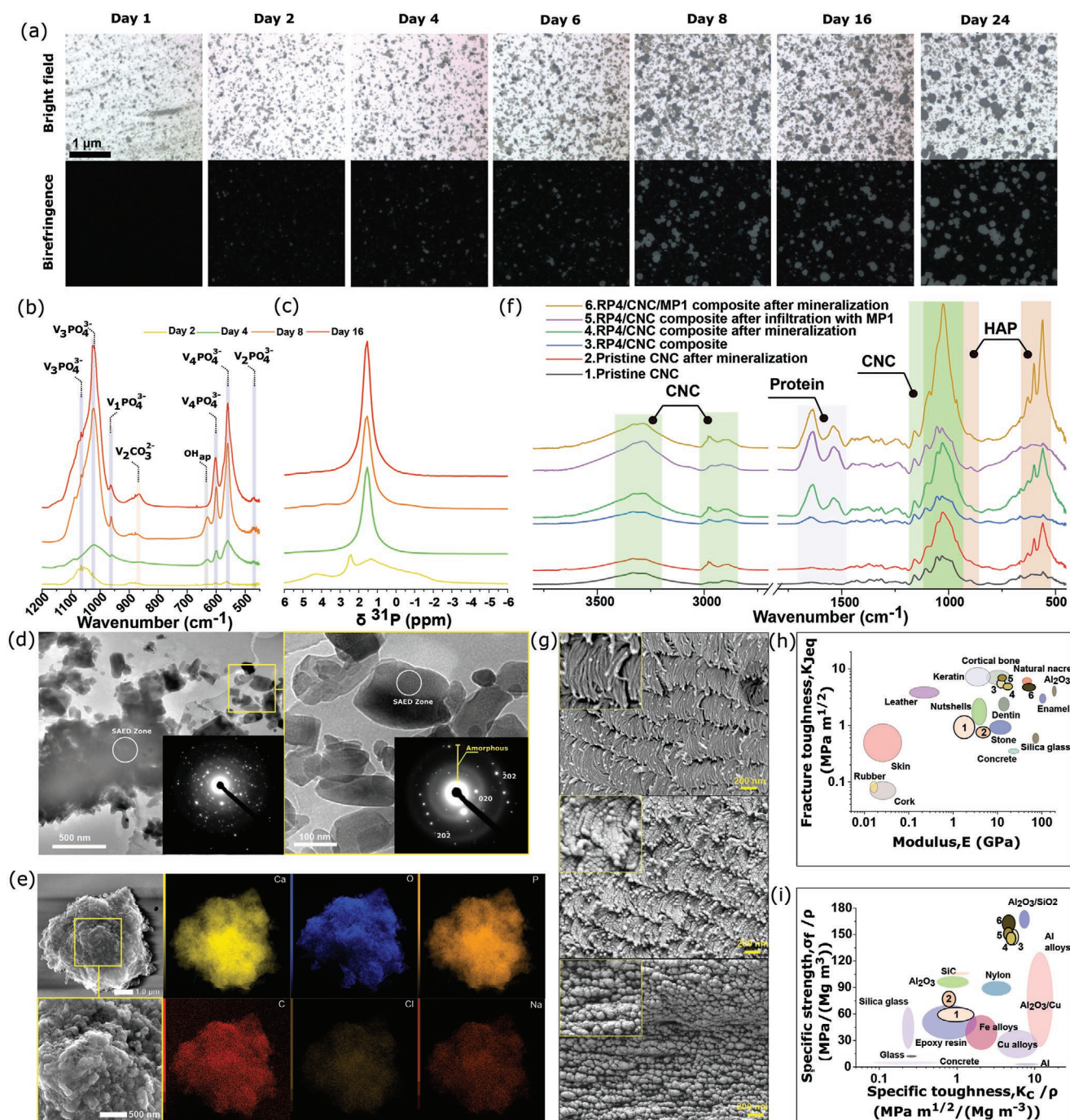
Figure 4. Apatite biomineralization and its effect on the mechanical properties of the bulk nanocomposite. a) LLPS of MP1 and apatite biomineralization for 30 d (Scale bar: 1 µm). b) ATR-FTIR spectrum of mineralized specimens incubated for 2, 4, 8, and 16 d. c) Solid-state ^{31}P CP/MAS spectrum of samples as in (b). d) TEM images of mineralized HAP granules formed after 16 d of incubation at various magnifications and corresponding selected-area electron diffractogram (SAED). e) EDS elemental maps of similar samples as in (d). f) 1) Raman spectra for pristine CNC, 2) pristine CNC after mineralization, 3) RP4/CNC, 4) RP4/CNC after mineralization, 5) RP4/CNC after infiltration with MP1, and 6) RP4/CNC/MP1 after mineralization. g) From top to bottom, SEM images of fractured cross-sections for samples 1, 4, and 6 in (f) after three-point flexural bending testing (scale bar: 200 nm). h,i) Ashby plots: h) K_{Jeq} versus modulus and i) specific strength versus specific K_{Ic} corresponding to (f). The plot also shows the comparison to a wide range of natural and engineered structural materials including human teeth.

coacervate state (RP4/CNC/MP1) was the most prominent among all the samples in terms of mineral assembly. Although there were slight shifts in the peak positions, the overall Raman spectrum was similar to the mineral phase formed in the solution. High-resolution SEM images also confirmed the formation of larger crystals at the interface of CNCs and this composite exhibited the most significant enhancement in mechanical properties with a modulus of 34 GPa and flexural strength

of 164 MPa (Figure 4h,i). These properties are similar to naturally occurring impact-resistant structural materials, including dentin, enamel, nacre and cortical bone (see Figure 4h,i).

These findings imply that sequestration of MP1 on the surface of the helicoidally organized RP4/CNC 3D scaffold could induce biomimetic apatite mineralization and emulate the highly mineralized stiff and hard exterior impact region of the dactyl club. Thus, CNCs bearing negatively charged carboxyl groups synergistically work in concert with MP1 to enhance sequestration of inorganic ions and apatite crystallization, therefore improving surface hardening. Recent findings also support our observation that HAP can form granule shapes with isotopic distribution on the surface of the anisotropic chitin–protein scaffold in the bulk of the highly mineralized exterior region of the club.[41]

2.4. Design and Fabrication of a Bioinspired Dental Implant Crown

As a proof of concept, we applied our two-component phase separating system to produce a functionally graded material replicating the complex shape of human teeth, with material properties suitable for use as a dental implant crown (**Figure 5**).
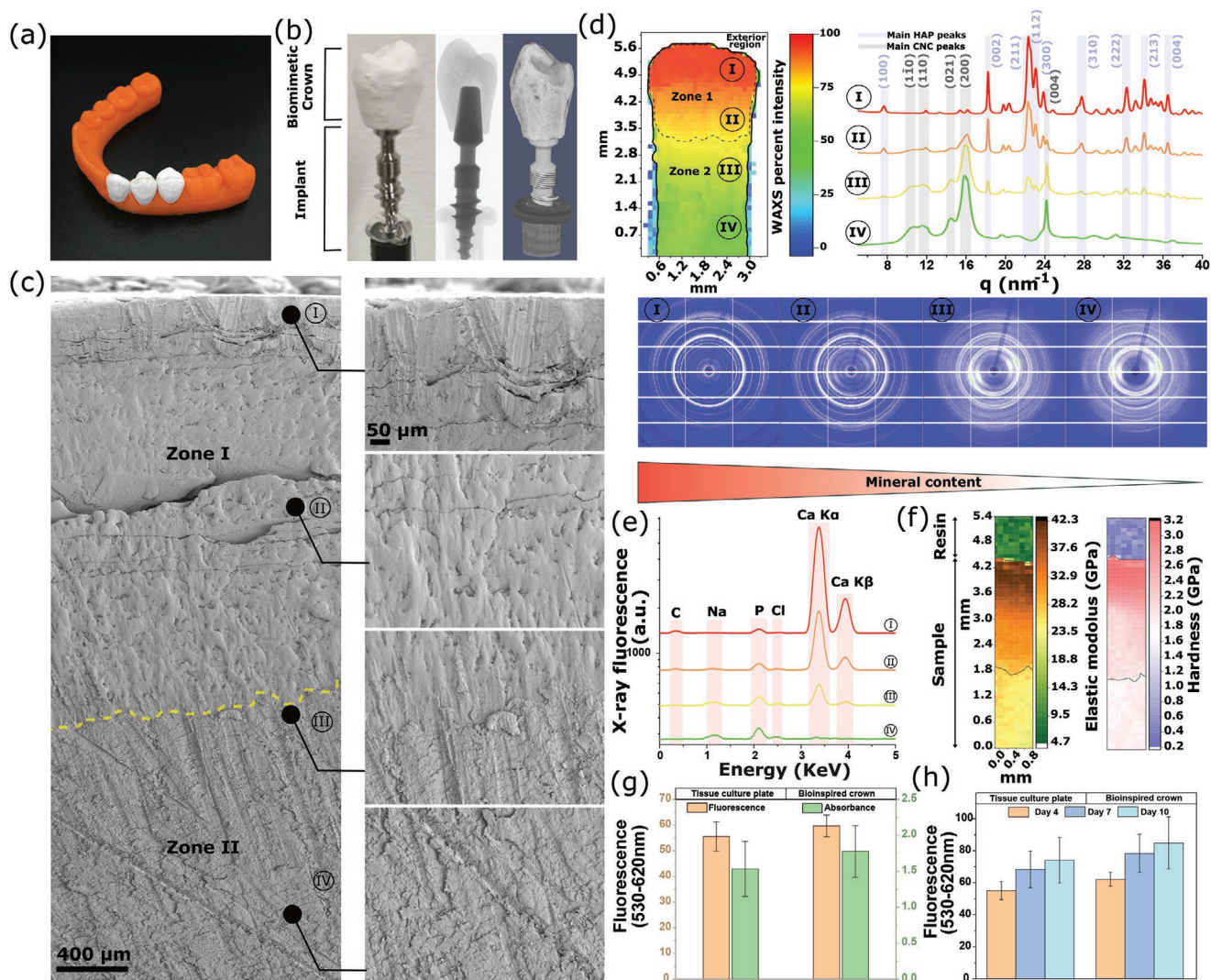

Figure 5. Bioinspired dental implant crown design, architecture, and composition. a) Front view of 3D-printed human lower jaw (orange) with canine, first, and second premolar bioinspired crowns in place (white). b) Side view of second premolar implant assembled from titanium screw with the bioinspired crown. The X-ray and μCT 3D tomogram images, respectively, are also illustrated. c) SEM images of cross-sections cut from the exterior to the interior of the crown indicating distinct microstructural regions. d) Synchrotron 2D WAXS mapping corresponding to regions shown in (c). The color indicates the intensity of the WAXS signal normalized to the most intense HAP peak. Representative 1D and 2D scattering plots corresponding to the four distinct microstructural regions are also shown. Major HAP and CNC peaks are indicated. e) Synchrotron X-ray fluorescence spectra in different regions shown in (c). f) Large-area ($L \approx 5.5$ mm, $W \approx 0.9$ mm) 2D nanoindentation map of elastic modulus and hardness for the cross-sectional cut from the exterior to the interior region of the crown. g,h) AB and LDH assay of adult human dermal fibroblast (AHDFs) cultured for 96 h on a tissue culture plate (TCP) and a bioinspired crown. Cell viability on both scaffolds over a period of 10 d is shown. No significant difference was found between the two samples (analysis of variance (ANOVA)/Tukey post hoc, *p*-value < 0.05).

**ADVANCED
SCIENCE NEWS**
www.advancedsciencenews.com

**ADVANCED
MATERIALS**
www.advmat.de

We began with a CNC hydrogel (80% dry w/v) to which RP4 was added (10%). The mixture was injected into custom-made crown molds and dried under pressure at 60 °C (Figure S22, Supporting Information) to form a canine, a first pre-molar, and a second pre-molar (details of the manufacturing steps included in the supplementary information). These resulting crowns exhibited a closely matched shape resemblance to their natural counterparts, including the finer morphological details (Figure 5a,b and Video S1, Supporting Information). To verify that a gradient of structural and mechanical properties from the exterior to the interior of the material was achieved, a brick-shaped sample was cut from the crown (Figure 5b) and imaged by SEM (Figure 5c) and phase mapping. Simultaneous WAXS diffraction patterns and X-ray fluorescence spectra from the exterior region showed an exceptionally high degree of crystallinity, with HAP as the dominant mineral phase as evidenced from the high intensity of the major reflections (002), (211), and (112) (Figure 5d) and the Ca Kα/Kβ signals (Figure 5e). Moving from the exterior to the interior region of the crown, a gradual decrease in the mineral phase was observed, until only the diffraction pattern and fluorescence signal corresponding to the protein/CNC mixture was detected, which remained constant throughout the rest of the interior region. This resulted in distinct and clearly delineated microstructural regions as observed by SEM (Figure 5c). The formation of the observed functional gradient was mediated through the biomineralization of the HAP and its accumulation throughout the "bulk" CNC-RP4-MP1 scaffold. The decrease in the mineral phase moving from the exterior to the interior region of the bulk scaffold occurs due to restricted diffusion of the mineralization solution.

The microstructural gradient was then correlated to the mechanical properties by conducting nanoindentation mapping of the entire crown (Figure 5f). Accordingly, the outermost region was the stiffest and hardest, with the elastic modulus ranging from ≈25 to 36 GPa and the hardness from 1.9 to 3.2 GPa, respectively. In contrast, the interior region was more compliant (elastic modulus 18 to 22 GPa) and softer (hardness 1.5–1.7 GPa.). Comparing the obtained values to the bilayered structure of the natural human tooth, we found a similar trend, with elastic and hardness values of 70–80 GPa and 4–4.5 GPa for the enamel (exterior layer of the natural tooth) and 15–20 and 0.5–0.8 GPa for dentine (interior region).[42] We finally performed an in vitro cytocompatibility assessment on the surface of the crown by culturing adult human dermal fibroblasts (AHDFs) (purchased from Sigma-Aldrich, product number 106-05A) on the surface of a 2D film with the same composition as the outer surface of the bioinspired crown (Figure 5g,h). The assays included cell viability and proliferation as well as cytotoxicity using Alamar Blue and lactate dehydrogenase. The surface material of the bioinspired crown could support the adhesion, growth, and proliferation of AHDFs without any apparent cytotoxicity, with no significant differences compared to the control tissue culture plate.

3. Conclusion

We have designed a bioinspired and robust mineralized composite constructed from building blocks that closely mimic those found in natural biomineralized materials. The starting matrix consists of CNCs self-assembled into a 3D chiral nematic scaffold, which is subsequently mixed with a family of genetically engineered, multidomain proteins rationally designed to bind CNCs and subsequently regulate nucleation and growth of HAP crystals. Critically, LLPS is also encoded in the proteins' primary structure, resulting in highly concentrated yet liquid-like coacervate microdroplets with superior wetting properties to infiltrate the CNC scaffold. The resulting bioinspired composite exhibits a graded microstructure with a correlated mechanical gradient that closely resembles those observed in natural biomineralized composites such as human teeth or the stomatopod dactyl club. To the best of our knowledge, the ability to regulate the growth of HAP crystals within the chiral nematic structure of CNCs using mineralizing domains to achieve both a graded microstructural design as well as surface hardening has not been previously achieved in engineered composites. Future developments will include scaling-up of material fabrication and prototyping for orthopedic applications, bone repair, and bioengineering.[43,44]

Supporting Information

Supporting Information is available from the Wiley Online Library or from the author.

Acknowledgements

Conflict of Interest

The authors declare no conflict of interest.

Data Availability Statement

The data that support the findings of this study are available from the corresponding author upon reasonable request.

Keywords

**ADVANCED
SCIENCE NEWS**

www.advancedsciencenews.com

**ADVANCED
MATERIALS**

www.advmat.de

[1] W. Yang, I. H. Chen, B. Gludovatz, E. A. Zimmermann, R. O. Ritchie, M. A. Meyers, *Adv. Mater.* **2013**, *25*, 31.

[2] W. Huang, D. Restrepo, J. Jung, F. Y. Su, Z. Liu, R. O. Ritchie, J. McKittrick, P. Zavattieri, D. Kisailus, *Adv. Mater.* **2019**, *31*, 1901561.

[3] Z. Liu, Z. Zhang, R. O. Ritchie, *Adv. Mater.* **2018**, *30*, 1705220.

[4] U. G. K. Wegst, H. Bai, E. Saiz, A. P. Tomsia, R. O. Ritchie, *Nat. Mater.* **2015**, *14*, 23.

[5] S. E. Naleway, M. M. Porter, J. McKittrick, M. A. Meyers, *Adv. Mater.* **2015**, *27*, 5455.

[6] A. H. Hofman, I. A. van Hees, J. Yang, M. Kamperman, *Adv. Mater.* **2018**, *30*, 1704640.

[7] A. Velasco-Hogan, J. Xu, M. A. Meyers, *Adv. Mater.* **2018**, *30*, 1800940.

[8] Y. Yang, X. Song, X. Li, Z. Chen, C. Zhou, Q. Zhou, Y. Chen, *Adv. Mater.* **2018**, *30*, 1706539.

[9] C. Zhang, D. A. Mcadams, J. C. Grunlan, *Adv. Mater.* **2016**, *28*, 6292.

[10] H. L. Ferrand, F. Bouville, T. P. Niebel, A. R. Studart, *Nat. Mater.* **2015**, *14*, 1172.

[11] S. Amini, A. Masic, L. Bertinetti, J. S. Teguh, J. S. Herrin, X. Zhu, H. Su, A. Miserez, *Nat. Commun.* **2014**, *5*, 3187.

[12] J. C. Weaver, G. W. Milliron, A. Miserez, K. Evans-Lutterodt, S. Herrera, I. Gallana, W. J. Mershon, B. Swanson, P. Zavattieri, E. DiMasi, *Science* **2012**, *336*, 1275.

[13] S. Amini, M. Tadayon, S. Idapalapati, A. Miserez, *Nat. Mater.* **2015**, *14*, 943.

[14] S. Amini, M. Tadayon, J. J. Loke, A. Kumar, D. Kanagavel, H. L.e Ferrand, M. Duchamp, M. Raida, R. M. Sobota, L. Chen, *Proc. Natl. Acad. Sci. USA* **2019**, *116*, 8685.

[15] S. Ling, D. L. Kaplan, M. J. Buehler, *Nat. Rev. Mater.* **2018**, *3*, 18016.

[16] M. V. Ramiah, D. A. I. Goring, *J. Polym. Sci., Part C: Polym. Symp.* **1965**, *11*, 27.

[17] T. Saito, R. Kuramae, J. Wohlert, L. A. Berglund, A. Isogai, *Biomacromolecules* **2013**, *14*, 248.

[18] S. F. Plappert, J.-M. Nedelec, H. Rennhofer, H. C. Lichtenegger, F. W. Liebner, *Chem. Mater.* **2017**, *29*, 6630.

[19] A. Dufresne, *Mater. Today* **2013**, *16*, 220.

[20] Y. Habibi, L. A. Lucia, O. J. Rojas, *Chem. Rev.* **2010**, *110*, 3479.

[21] C. Honorato-Rios, J. P. F. Lagerwall, *Commun. Mater.* **2020**, *1*, 69.

[22] P.-X. Wang, W. Y. Hamad, M. J. MacLachlan, *Nat. Commun.* **2016**, *7*, 11515.

[23] P. Mohammadi, A. S. Aranko, C. P. Landowski, O. Ikkala, K. Jaudzems, W. Wagermaier, M. Linder, *Sci. Adv.* **2019**, *5*, eaaw2541.

[24] P. Mohammadi, J. Christopher, G. Beaune, P. Engelhardt, A. Kamada, J. V. I. Timonen, T. P. J. Knowles, M. Penttila, M. B. Linder, *J. Colloid Interface Sci.* **2020**, *560*, 149.

[25] P. Mohammadi, A. S. Aranko, L. Lemetti, Z. Cenev, Q. Zhou, S. Virtanen, C. P. Landowski, M. Penttilä, W. J. Fischer, W. Wagermaier, M. B. Linder, *Commun. Biol.* **2018**, *1*, 86.

[26] P. Mohammadi, G. Beaune, B. T. Stokke, J. V. I. Timonen, M. B. Linder, *ACS Macro Lett.* **2018**, *7*, 1120.

[27] S. Y. Bahn, B. H. Jo, Y. S. Choi, H. J. Cha, *Sci. Adv.* **2017**, *3*, e1700765.

[28] Y. Tan, S. Hoon, P. a Guerette, W. Wei, A. Ghadban, C. Hao, A. Miserez, J. H. Waite, *Nat. Chem. Biol.* **2015**, *11*, 488.

[29] F. Jehle, E. Macías-Sánchez, P. Fratzl, L. Bertinetti, M. J. Harrington, *Nat. Commun.* **2020**, *11*, 862.

[30] Y. Sun, Z. W. Lim, Q. Guo, J. Yu, A. Miserez, *MRS Bull.* **2020**, *45*, 1039.

[31] T. Yoshioka, T. Tsubota, K. Tashiro, A. Jouraku, T. Kameda, *Nat. Commun.* **2019**, *10*, 1469.

[32] S. Roberts, T. S. Harmon, J. L. Schaal, V. Miao, K. J. Li, A. Hunt, Y. Wen, T. G. Oas, J. H. Collier, R. V. Pappu, *Nat. Mater.* **2018**, *17*, 1154.

[33] B. Gabryelczyk, H. Cai, X. Shi, Y. Sun, P. J. M. Swinkels, S. Salentinig, K. Pervushin, A. Miserez, *Nat. Commun.* **2019**, *10*, 5465.

[34] W. Fang, M. V. Nonappa, P. Mohammadi, S. Koskela, M. Soikkeli, A. Westerholm-Parvinen, C. P. Landowski, M. Penttilä, M. B. Linder, P. Laaksonen, *Colloids Surf., B* **2018**, *171*, 590.

[35] A. Rising, J. Johansson, *Nat. Chem. Biol.* **2015**, *11*, 309.

[36] N. Suksangpanya, N. A. Yaraghi, R. B. Pipes, D. Kisailus, P. Zavattieri, *Int. J. Solids Struct.* **2018**, *150*, 83.

[37] S. Elsharkawy, M. Al-Jawad, M. F. Pantano, E. Tejeda-Montes, K. Mehta, H. Jamal, S. Agarwal, K. Shuturminska, A. Rice, N. V. Tarakina, *Nat. Commun.* **2018**, *9*, 2145.

[38] R. Mathew, C. Turdean-Ionescu, Y. Yu, B. Stevensson, I. Izquierdo-Barba, A. García, D. Arcos, M. Vallet-Regí, M. Edén, *J. Phys. Chem. C* **2017**, *121*, 13223.

[39] Y. Wang, S. Von Euw, F. M. Fernandes, S. Cassaignon, M. Selmane, G. Laurent, G. Pehau-Arnaudet, C. Coelho, L. Bonhomme-Coury, M.-M. Giraud-Guille, *Nat. Mater.* **2013**, *12*, 1144.

[40] S. V. Dorozhkin, *Acta Biomater.* **2010**, *6*, 4457.

[41] N. A. Yaraghi, N. Guarín-Zapata, L. K. Grunenfelder, E. Hintsala, S. Bhowmick, J. M. Hiller, M. Betts, E. L. Principe, J. Jung, L. Sheppard, *Adv. Mater.* **2016**, *28*, 6835.

[42] Z. Wang, K. Wang, W. Xu, X. Gong, F. Zhang, *Dent. Mater.* **2018**, *34*, 376.

[43] W. He, A. K. Rajasekharan, A. R. Tehrani-Bagha, M. Andersson, *Adv. Mater.* **2015**, *27*, 2260.

[44] L.-B. Mao, H.-L. Gao, H.-B. Yao, L. Liu, H. Cölfen, G. Liu, S.-M. Chen, S.-K. Li, Y.-X. Yan, Y.-Y. Liu, *Science* **2016**, *354*, 107.